

## CHAPTER 4

### NICKEL AND COBALT MAGNETIC MATERIAL CHARACTERIZATION

High-sensitivity magnet-on-cantilever MRFM requires that nanoscale magnetic tips at the leading edge of attonewton-sensitivity cantilevers be well-magnetized and have high saturated magnetic moments. A process to fabricate nanomagnet-tipped chips and attach them to cantilevers was presented in Chapter 3. Scanning electron microscopy (SEM) images indicated that the nanomagnets were fabricated with high yield.

This chapter summarizes work conducted to analyze the magnetization and elemental composition of nickel and cobalt nanomagnets, as well as large-area thin magnetic films. Frequency-shift cantilever magnetometry was conducted to provide estimates of the magnetization of individual nanomagnets with dimensions of approximately  $100\text{nm} \times 100\text{nm} \times 1.5\mu\text{m}$ . Initial cantilever magnetometry studies indicated that the nickel nanomagnets exhibited saturation magnetizations that were significantly lower than the theoretical value for nickel of  $\mu_0 M_{\text{sat}} = 0.6$  T. To analyze potential sources of damage, superconducting quantum interference device (SQUID) magnetometry and X-ray photoelectron spectroscopy (XPS) with depth profiling were utilized. Key findings from this analysis led to adjustments of the nanomagnet fabrication process. Frequency-shift cantilever magnetometry conducted on a cobalt nanomagnet after the modifications were made indicated that the magnetization of the nanomagnet had a fully saturated magnetic moment.

#### 4.1 Initial Frequency-Shift Cantilever Magnetometry Studies on Nickel Nanomagnets

Frequency-shift cantilever magnetometry is one of the few techniques that is capable of determining the average magnetization of individual sub-micrometer magnetic particles [81, 89,

[93, 117]. Frequency-shift cantilever magnetometry was used to calculate the saturation magnetization of overhanging nickel nanomagnets on silicon chips that were prepared using the original magnet-tipped fabrication protocol detailed in Section 3.2. Six nickel nanomagnet-tipped chips were attached to cantilevers by the focused ion beam (FIB) lift-out method (Section 3.4) prior to cantilever magnetometry analysis.

These nickel nanomagnets had widths of either 120 nm or 220 nm and were either non-overhanging or had an overhang of approximately 300 nm (Table 4.1). Magnetometry experiments were conducted on a custom-built probe operating at  $T = 4.2\text{ K}$  and  $P = 10^{-6}\text{ mbar}$ . Changes in cantilever frequency were measured as an external magnetic field applied along the long axis of the magnet was swept between  $-4\text{ T}$  and  $+4\text{ T}$ . Cantilever motion was monitored using a fiber-optic interferometer (wavelength  $\lambda = 1310\text{ nm}$  and power  $P \approx 3\text{ }\mu\text{W}$ ). During the measurement, the cantilever was forced to self oscillate at a root mean square (RMS) amplitude of approximately 90 nm. Self oscillation was achieved by using the cantilever as the frequency determining element of a proportional-integral-controlled-gain positive feedback circuit that drove a piezoelectric element located under the cantilever base. The cantilever frequency was determined by digitizing the interferometer output and using a software frequency demodulator [85]. Spring constant changes  $\Delta k$  were computed from frequency shifts  $\Delta f$  using  $\Delta k = 2k\Delta f/f_0$  with  $k$  and  $f_0$  the cantilever spring constant and resonance frequency, respectively. The spring constant was determined from the mean square displacement of the undriven cantilever at a temperature  $T = 4.2\text{ K}$  [138]. Cantilever dissipation was inferred from either the cantilever ringdown time or by following the gain control of the positive feedback loop. The magnetic moment of the nanomagnet was extracted by fitting the spring constant shift versus magnetic field data to [89, 93, 139]:

$$\frac{\Delta k}{k} = \frac{\mu_{\text{sat}}}{k} \left( \frac{\alpha}{l} \right)^2 \frac{B\Delta B}{B + \Delta B}. \quad (4.1)$$

with  $\mu_{\text{sat}}$  the saturated magnetic moment,  $\alpha = 1.377$  a constant dependent on the cantilever mode shape,  $l$  the cantilever length,  $B = \mu_0 H$  the applied magnetic field, and  $\Delta B =$

$\mu_0\mu_{\text{sat}}\Delta N/V$ , where  $\mu_0$  is the permeability of free space and  $\Delta N = N_t - N_l$  is the difference in demagnetization factor along the cantilever's thickness and length, respectively. The volume  $V$  of the nanomagnet was computed from estimates of the magnet's lateral dimensions (obtained from SEM images) and thickness (measured for one representative sample using atomic force microscopy). Fractional cantilever frequency shift as a function of applied magnetic field is shown in Fig. 4.1<sup>1</sup> for the magnet on cantilever C1, which had a 220 nm wide overhanging magnet. The parameters  $\mu_{\text{sat}}$  and  $\Delta N$  were obtained from a non-linear least-squares fit of the frequency-shift data to Eq. 4.1, and the magnetization  $\mu_0 M_{\text{sat}}$  was computed using  $\mu_0 M_{\text{sat}} = \mu_0\mu_{\text{sat}}/V$ . Fit results are shown in Table 4.1, and the nominal saturated magnetic moment  $\mu_{\text{sat}}^{\text{nominal}}$ , which was calculated for fully-magnetized nickel particles of the same measured dimensions, is provided for comparison. For one magnet, indicated in the table, the fit was too poor to accurately obtain all three parameters from the frequency-shift data; in this case,  $\Delta N$  was calculated from the estimated length and thickness using demagnetization factors obtained by Aharoni for a rectangular prism [140], and  $\mu_{\text{sat}}$  and  $V$  were obtained by fitting.

The data in Table 4.1 indicate that the net magnetization of each of the six nickel nanomagnets studied was lower than the theoretical value for bulk nickel. Two magnets with widths of 120 nm, C2 and C3, were studied. When compared to the saturation magnetization  $\mu_0 M_{\text{sat}} = 0.6$  T of bulk nickel [91], the saturation magnetization for C2 and C3 were  $42\% \pm 5\%$  and  $59\% \pm 12\%$  of the expected value, respectively. Four 220 nm wide nanomagnets were studied: C1, C4, C5, and C6. All of the 220 nm wide nanomagnets exhibited saturation magnetizations that were more than 50% of the value for bulk nickel; the average saturation magnetization was  $63\% \pm 10\%$ , and the best-magnetized magnet (on C6) was  $79\% \pm 11\%$  magnetized. Here the standard error in  $\mu_0 M_{\text{sat}}$  is reported as an indication of the goodness of fit; note that the true error in  $\mu_0 M_{\text{sat}}$  is dominated by the uncertainty in measuring  $k$ , which

---

<sup>1</sup>Figure 4.1 and Table 4.1 reprinted with permission from J. G. Longenecker *et al.*, J. Vac. Sci. Technol. B **29**, 032001 (2011). Copyright 2011, American Vacuum Society.

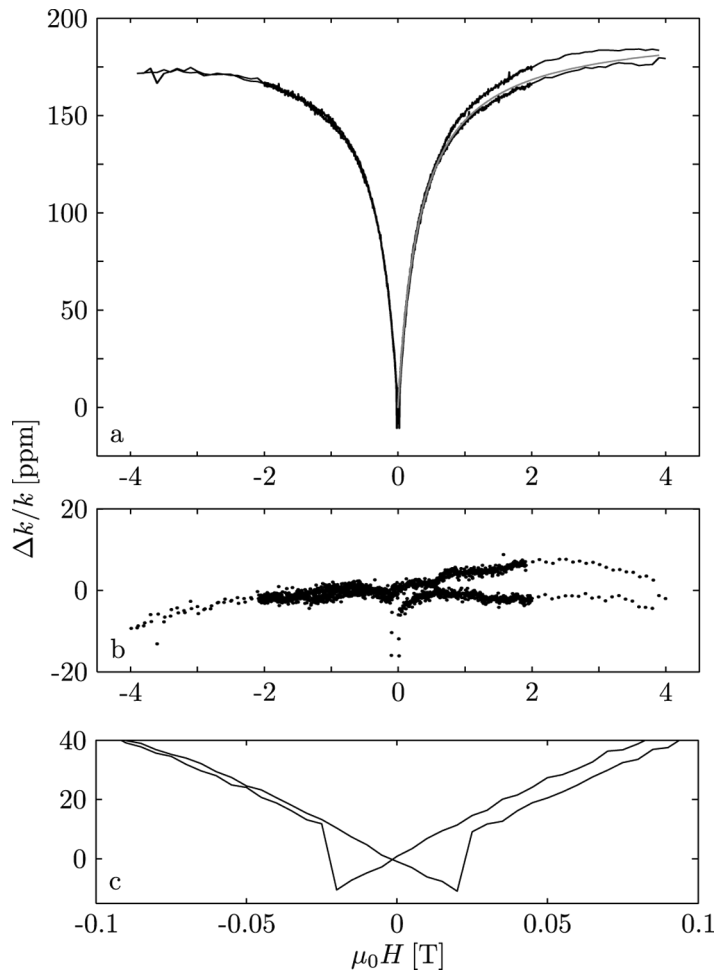


Figure 4.1: Frequency-shift cantilever magnetometry for the 220 nm wide nickel nanomagnet on cantilever C1. The applied external field was aligned parallel to the length of the nanomagnet. Upper: Data (solid; black) and best-fit to Eq. 4.1 (dotted; gray). Middle: Fit residuals, shown for an applied field ranging from  $-4$  T to  $+4$  T. Lower: Magnified view of the hysteresis present near zero field, indicating single-domain switching with a coercive field of  $H_c \approx 0.05$  T.

Table 4.1: Summary of cantilever and magnet properties. All cantilever properties were measured at a field of 0 T unless otherwise indicated. All of the cantilevers studied had dimensions of  $200\text{ }\mu\text{m} \times 4\text{ }\mu\text{m} \times 0.34\text{ }\mu\text{m}$ . Cantilever resonance frequencies were  $f_0 \approx 9000\text{ Hz}$  prior to adhesion of the magnet-tipped chips. The reported error bars represent a 95% confidence interval.

quantity	C1	C2	C3	C4	C5	C6	C7	unit
$f_0$	6631	6053	5054	6486	5351	4838	5695	Hz
$Q$ (at 0 T)	67,900	74,400	41,000	86,700	43,200	94,000	49,800	(unitless)
$Q$ (at 5 T)	68,600	75,500	39,600	84,200	41,600			(unitless)
$k$	780	500	$563 \pm 63$	780	780	$703 \pm 52$	$764 \pm 61$	$\times 10^{-6}\text{ N m}^{-1}$
$\Gamma$	275	177	432	221	537	246	429	$\times 10^{-15}\text{ N s m}^{-1}$
$F_{\min}$	8.0	6.4	10.0	7.2	11.2	7.6	10.0	$\times 10^{-18}\text{ N}$
$l_m$	1500	1500	1500	1500	1500	1500	1500	mm
$l_{\text{overhang}}$	$\sim 300$	$\sim 300$	$\sim 300$	$\sim 300$	0	0	0	mm
$w_m$	220	120	120	220	220	220	220	mm
$t_m$	90	90	90	90	90	90	90	nm
$\mu_{\text{sat}}$	$9.71 \pm 0.98$	$4.50 \pm 0.90$	$3.21 \pm 0.30$	$9.08 \pm 1.36$	$9.05 \pm 1.43$	$11.72 \pm 1.27$	$8.83 \pm 0.72$	$\times 10^{-15}\text{ A m}^{-2}$
$\mu_0 M_{\text{sat}}$	$0.41 \pm 0.04$	$0.35 \pm 0.07$	$0.25 \pm 0.03$	$0.38 \pm 0.06$	$0.38 \pm 0.06$	$0.49 \pm 0.08$	$0.37 \pm 0.03$	T
$\Delta N$	$0.81 \pm 0.08$	$0.51^a$	$0.93 \pm 0.10$	$0.99 \pm 0.15$	$0.86 \pm 0.15$	$0.40 \pm 0.10$	$0.70 \pm 0.06$	(unitless)
$\mu_{\text{sat}}^{\text{nominal}}$	14.18	7.73	7.73	14.18	14.18	14.18	14.18	$\times 10^{-15}\text{ A m}^{-2}$

<sup>a</sup> For this fit,  $\Delta N$  was calculated from the magnet shape as described in the text.

could be 40% or larger. As discussed further in Section 4.5, this large experimental error is due to the inability to localize the position of the laser interferometer on the cantilever pad (see Figure 3.4) to better than within  $\pm 15 \mu\text{m}$ .

In summary, frequency-shift magnetometry conducted on 120 and 220 nm wide magnets indicated that the nanomagnets exhibited saturation magnetizations that were lower than the value for bulk nickel. Even considering the large 40% uncertainty in the spring constant, the magnetization of most of the tips is lower than the expected  $\mu_0 M_{\text{sat}} = 0.60 \text{ T}$ . The reduced-magnetization results presented in Table 4.1 would be consistent with the presence of a uniform-thickness damage shell of approximately 16 nm. By studying both overhanging (C1-C4) and non-overhanging (C5-C6) nanomagnets, it was determined that the saturation magnetization of the nanomagnets was unaffected by the fabrication steps required to produce overhanging magnets. The cantilever quality factor was not measured to have a strong dependence on applied magnetic field; representative shifts in an applied field of 5 T are reported in Table 4.1.

## 4.2 Hypotheses to Explain the Low Magnetization of the Nickel Nanomagnets

The low saturated magnetic moments of the nickel nanomagnets measured by frequency-shift cantilever magnetometry in Section 4.1 were a surprising finding because they could not be attributed to process incompatibilities. Nickel oxidation could not account for a 16 nm thick shell of damage since nickel is well-documented to not form an oxide that is thicker than 1 to 2 nm near room temperature and atmospheric pressure [110–112, 141]. Damage due to silicide formation during the evaporation of hot nickel onto the silicon substrate also was unlikely; electron energy loss spectroscopy (EELS) did not indicate the presence of any

silicon in the overhanging component of the nickel nanomagnet studied in Chapter 2, and it has been reported that the native  $\text{SiO}_2$  layer on a silicon surface is sufficient to prevent nickel silicidation during deposition of the magnetic material [103]. Additionally, the FIB attachment procedure was not indicated to be a source of magnet damage. Frequency-shift cantilever magnetometry characterization was conducted on a seventh magnet-tipped cantilever (C7 in Table 4.1) that had a nickel nanomagnet coated with 10 nm of platinum. The saturation magnetization of C7 was comparable to other 220 nm wide magnets, indicating that coating with a protective layer did not change the magnetization. If the damage had been due to ion-beam exposure at 30 kV, significant gallium implantation damage should have damaged the top 10 nm of the film and a difference in magnetization would have been observed between the platinum-capped and uncapped nanomagnets.

It was also considered whether the low magnetization could have resulted from a faulty assumption about the planarity of the cantilevers. It has been observed that some of the custom-fabricated silicon cantilevers have a downward bend of a few degrees near the leading edge (Figure 4.2). In the frequency-shift cantilever magnetometry measurements in Section 4.1, it was assumed that the longest axis of the nanomagnet (the 1.5  $\mu\text{m}$  length) was parallel to the applied external field. Since the long axis of the nanomagnet lies along the length of the cantilever, a bend in the cantilever would have introduced an offset angle between the nanomagnet and the applied external field. Frequency-shift magnetometry simulations were carried out for offset angles ranging from  $\alpha = 0^\circ$  to  $\alpha = 45^\circ$ , as shown in Figure 4.3. It was determined that the cantilever would need to be bent by at least  $30^\circ$  to account for the reduction of magnetization observed in Section 4.1; the observed bending of less than  $10^\circ$  in Figure 4.2 would at most account for a 5% error in the saturation magnetization.

Since the error in the spring constant  $k$  could be as large as 40%, it is possible that almost

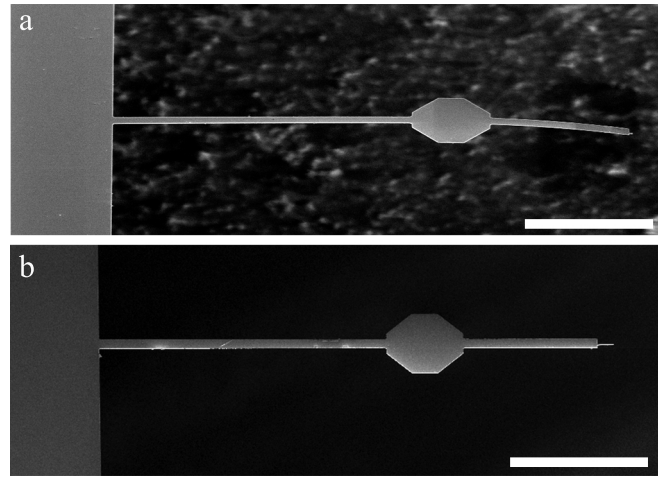


Figure 4.2: SEM images of attonewton-sensitivity cantilevers. (a)  $52^\circ$  tilted image of a cantilever that is bent by a few degrees. (b)  $30^\circ$  tilted image of a straight cantilever. Both scale bars represent  $50 \mu\text{m}$ .

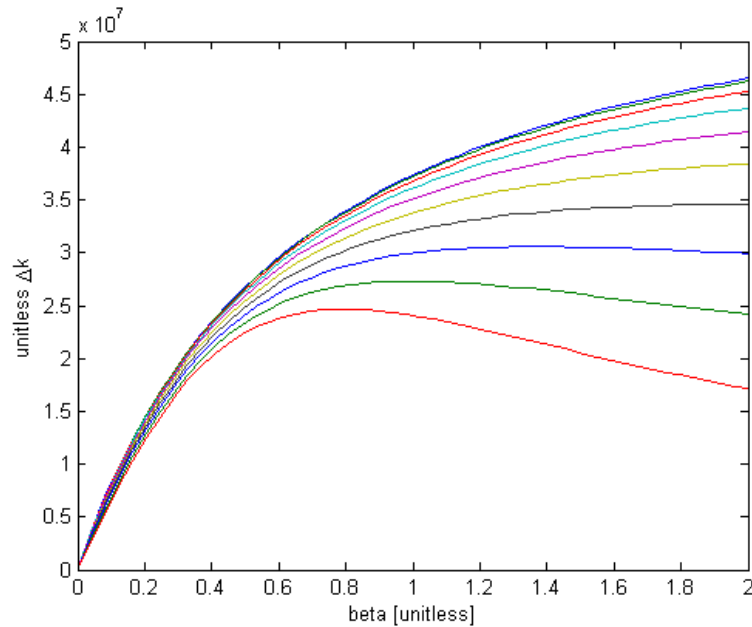


Figure 4.3: Frequency-shift cantilever magnetometry simulations to assess the effect of cantilever bending. Offset angles between the long axis of the nanomagnet/cantilever and the applied field were simulated between angles of  $0^\circ$  (top line) to  $45^\circ$  (bottom line) in increments of  $5^\circ$ . The simulations indicate that offset angles larger than  $30^\circ$  (black line) would be required to account for the loss of magnetization observed in Section 4.1.

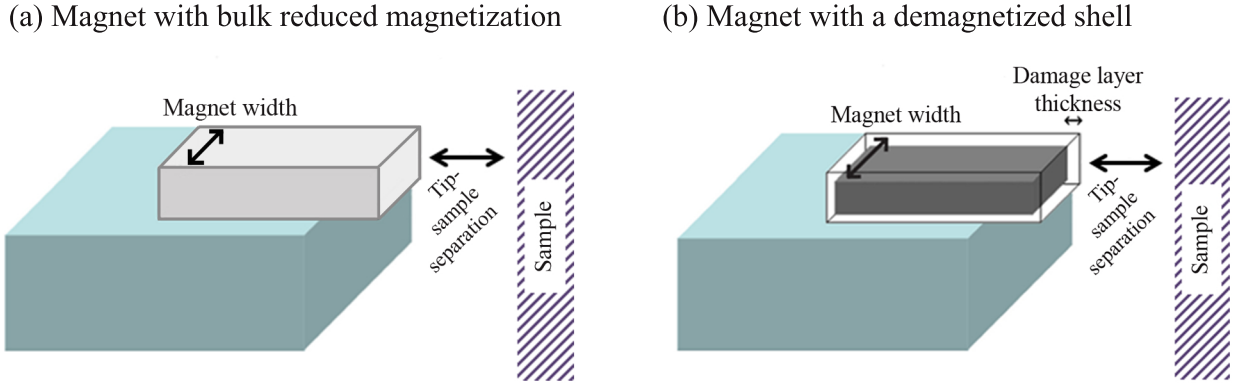


Figure 4.4: Illustrations of two proposed reduced-magnetization damage scenarios (hypotheses 1 and 2). (a) Bulk damage scenario in which the saturated magnetization of the nanomagnet is uniformly reduced; the reduced magnetization is represented as light gray. In this case, the tip-sample separation is the same as the spacing between the magnetic material and the sample surface. (b) Fully-magnetized nanomagnet core (dark gray) encased by a shell of non-magnetic material (white). In this case, the spacing between the magnetic material and the sample surface is equal to the sum of the tip-sample separation and the damage layer thickness.

all of the observed reduction of magnetization was due to poor measurement of  $k$ . However, two alternative fabrication-related explanations for the observed reduction in saturation magnetization were still possible and worthy of consideration: (1) the nickel films could have been contaminated by using the general-purpose evaporation chamber at the Cornell CNF nanofabrication facility, which possibly could have caused the formation of non-magnetic or antiferromagnetic regions and resulted in a roughly uniform reduction in magnetization, as illustrated in Figure 4.4(a); or (2) a damage layer of demagnetized material could have been formed as a shell around the nanomagnet, as illustrated in Figure 4.4(b).

### 4.3 Nickel and Cobalt Magnetic Material Analysis

SQUID and XPS data on nickel and cobalt films are presented to distinguish between hypotheses 1 and 2 from Section 4.2. Contamination of the bulk magnetic material (hypothesis 1) was tested by using SQUID magnetometry to study large-area thin films of nickel and

cobalt that were deposited using the same evaporation chamber that was used for the evaporation of the nickel nanomagnets in Section 4.1. Nickel and cobalt crucibles used for the evaporations were stored separately from the common-access crucibles in the cleanroom to avoid contamination of the metal targets. Surface contamination (hypothesis 2) was tested by performing elemental analysis of blanket-deposited thin films of nickel and cobalt using XPS in combination with depth profiling. Understanding the presence of any contamination at the leading edge of the nanomagnets was of particular importance since the nanomagnet leading edge is brought to within a few nanometers of a sample surface in MRFM experiments. At these small tip-sample separations, the experimental noise is dominated by non-contact friction interactions between the magnet-tipped cantilever and the surface [83, 84]. A non-magnetic layer at the leading edge of the nanomagnet would increase the distance between the nanomagnet and the sample spins, which would decrease the tip-field gradient and the signal-to-noise ratio of the MRFM signal.

### 4.3.1 SQUID Magnetometry Sample Preparation

Square and circular thin magnetic films were studied using SQUID magnetometry. Square films had lateral dimensions of 1.5 mm and circular films had a diameter of approximately 1.7 mm; all films covered an area of 2.25 mm<sup>2</sup>. All samples were prepared on 500  $\mu\text{m}$  thick fused silica wafers. Fused silica had a low observed diamagnetic susceptibility, whereas p-type silicon wafers with a resistivity of 10 to 25  $\Omega\text{ cm}$  had a high magnetic susceptibility that overpowered the SQUID signal. A bilayer resist of LOR 10A below SPR 220-3 was spun on the wafer. The LOR 10A layer was spun at 500 rpm for 10 seconds, followed by spinning at 3000 rpm for an additional 45 seconds. Prior to depositing the second resist layer, the wafer was baked at 180°C for 5 minutes. The SPR 200-3 resist layer was spun at 3000 rpm for 30 seconds and the wafer was baked again at 115°C for 90 seconds. The

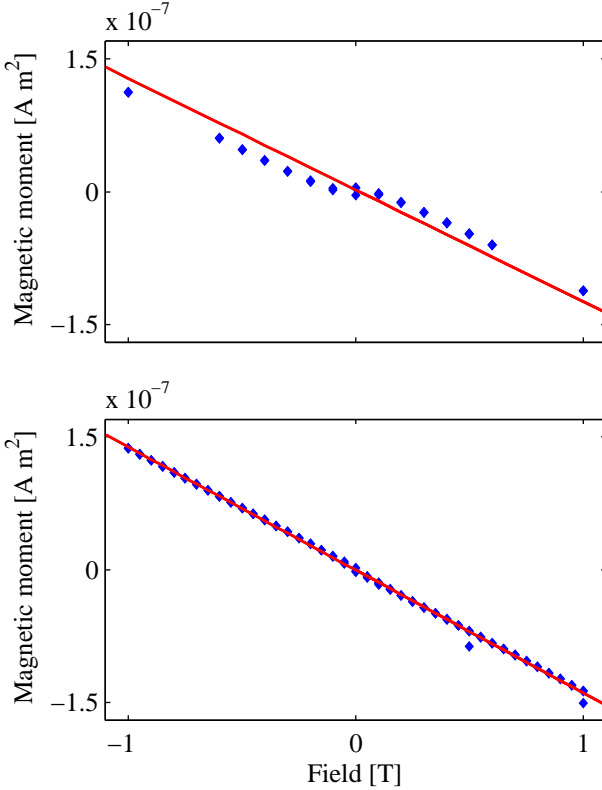


Figure 4.5: In-plane SQUID magnetization loops obtained at 4.0 K for blank fused silica chips that were handled with metal tweezers (top) or plastic tweezers (bottom). Metal tweezers were observed to induce ferromagnetic contamination of the fused silica substrate.

wafer was patterned on the ABM contact aligner; the exposure time was 12 seconds. The post exposure bake was at 115°C for 90 seconds. The patterned wafer was descummed for 60 seconds in an oxygen plasma using an Oxford PlasmaLab 80+ RIE System. The magnetic films were deposited using the same procedures as outlined in Sections 3.2 and 3.6. Nickel films (either 43 or 82 nm thick) or cobalt films (84 or 92 nm thick) were deposited on top of 5 nm thick chromium or titanium adhesion layers. In some cases, 10 nm of platinum was evaporated on top of the thin films. After lift-off, the wafers were diced into  $6.5 \times 6.5$  mm pieces using a KS 7100 Dicing Saw such that each chip contained one magnetic circle or square. The resulting chips were handled with plastic tweezers to minimize ferromagnetic contamination (Figure 4.5).

### 4.3.2 SQUID Magnetometry Analysis and Results

SQUID magnetometry was conducted using a Quantum Design MPMS-XL SQUID Magnetometer. Each chip was centered in a plastic drinking straw sample holder; the chip width was optimized to fit snugly in the drinking straw. The drinking straw was adhered to the end of a sample rod using Kapton tape, and the sample was inserted into the magnetometer. The system was cooled to 4.0 K in the absence of a magnetic field and was allowed to equilibrate for 30 minutes prior to data collection. Measurements were typically taken between either  $\pm 1.5$  T or  $\pm 3$  T, first sweeping positive to negative and then back from negative to positive fields.

The magnetic moment of each film was calculated by subtracting the linear diamagnetic background of the fused silica chip from the total signal. To convert to saturation magnetization, the magnetic moment was averaged in the saturated regime and was divided by the volume of the thin film sample. The film diameter (circle) or width (square) was measured by optical microscopy, and the thickness of the magnetic material was determined by using an *in situ* quartz crystal microbalance and carrying out atomic force microscope (AFM) profilometry on the sample edge.

Background-subtracted SQUID magnetometry data for circular platinum-capped nickel (TiNiPt) and uncapped nickel (TiNi) films, both with titanium adhesion layers, are shown in Figure 4.6. The platinum-capped nickel film was  $43 \pm 2$  nm thick and the uncapped film was  $82 \pm 4$  nm thick; both error bars represent a 95% confidence interval. The saturation magnetization was determined to be  $0.54 \pm 0.03$  T for the platinum-capped film and  $0.61 \pm 0.03$  T for the uncapped film. The saturation magnetization error bars represent 95% confidence intervals and account for the error in the nickel thickness, the nickel lateral dimensions, and the SQUID measurement. The saturation magnetizations of both the protected and unprotected nickel films are within reasonable agreement of the expected value for nickel of 0.6 T,

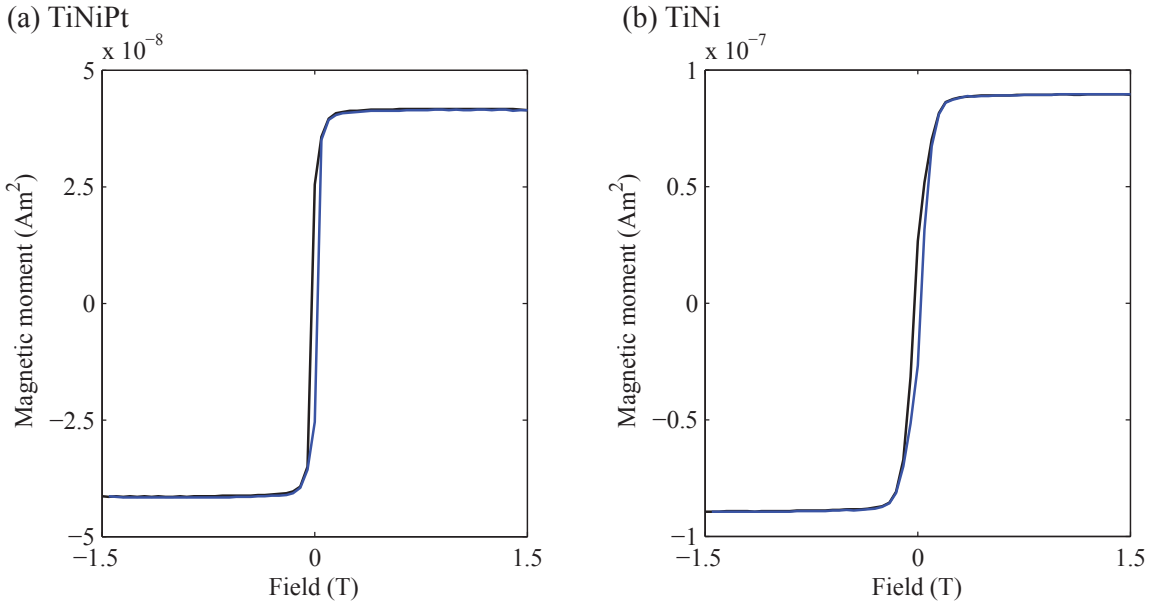


Figure 4.6: In-plane magnetization loops for two circular nickel films with titanium adhesion layers that were obtained at 4.0 K using SQUID magnetometry. The magnetization was swept from +1.5 T to −1.5 T (black) and then from −1.5 T to +1.5 T (blue). (a) Platinum-capped nickel film with an area of 2.25 mm<sup>2</sup> and a magnetic layer thickness of 43 nm. Given this volume, the observed saturated magnetic moment corresponds to a saturation magnetization  $\mu_0 M_{\text{sat}} = 0.54 \pm 0.03$  T. (b) Uncapped 82 nm thick nickel circular film that also had an area of 2.25 mm; the corresponding saturation magnetization is  $0.61 \pm 0.03$  T.

which indicates that there was minimal degradation or contamination of the nickel magnetic material.

It is important to note that the choice of adhesion layer material can play a critical role in the magnetization properties of the film. In Section 4.1 and in previous studies [68, 81, 89], 5 nm thick chromium adhesion layers were used and the magnetic contributions of the chromium layers were assumed to be negligible. In Figure 4.7, in-plane magnetization loops for two square nickel films with the same lateral dimensions and thicknesses are shown. The nickel film with the titanium adhesion layer (Figure 4.7(a)) displayed the expected saturation behavior. In contrast, the otherwise identical nickel film with a chromium adhesion layer (Figure 4.7(b)) exhibited anomalous behavior at high fields, which is attributed to interactions between the ferromagnetic cobalt and antiferromagnetic chromium or Cr<sub>2</sub>O<sub>3</sub>

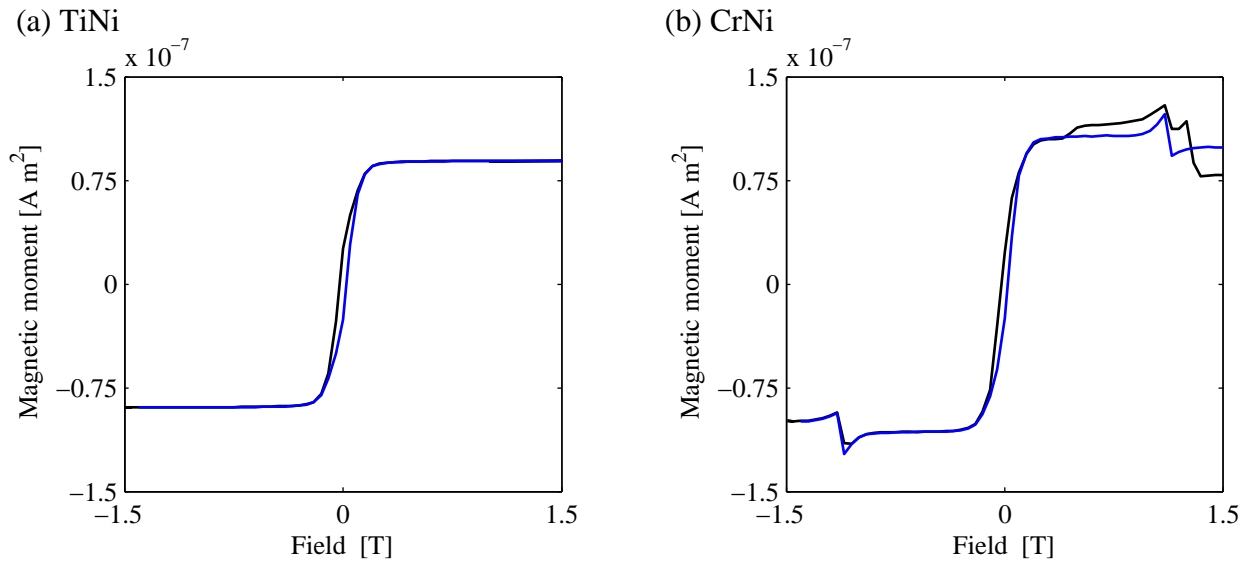


Figure 4.7: SQUID in-plane magnetization loops for nickel films with (a) titanium and (b) chromium adhesion layers. Measurements were conducted at 4.0 K. The magnetization was swept from +1.5 T to −1.5 T (black) and then from −1.5 T to +1.5 T (blue). Other than the choice of adhesion layer material, the films were nominally identical in area and thickness. The high-field magnetic behavior in panel (b) is attributed to the 5 nm thick chromium layer.

[133]. Because of these findings, all subsequent deposited magnetic films were evaporated with titanium adhesion layers.

Circular cobalt thin films with and without platinum capping layers were also studied by SQUID magnetometry. Both films were circular and had titanium adhesion layers. The platinum-capped cobalt film was  $84 \pm 5$  nm thick, and the uncapped film was  $92 \pm 4$  nm thick; both error bars represent a 95% confidence interval. The area of the platinum-capped film was straight-forward to calculate based on its thickness and area. The chip containing the uncapped film had residual magnetic material at the corners from dicing saw alignment marks that were not completely removed during dicing; the small combined area of these alignment marks (approximately 1% of the total area) was taken into account for the final volume of the uncapped sample.

After accounting for the volume of each film, the measured saturated magnetic moments

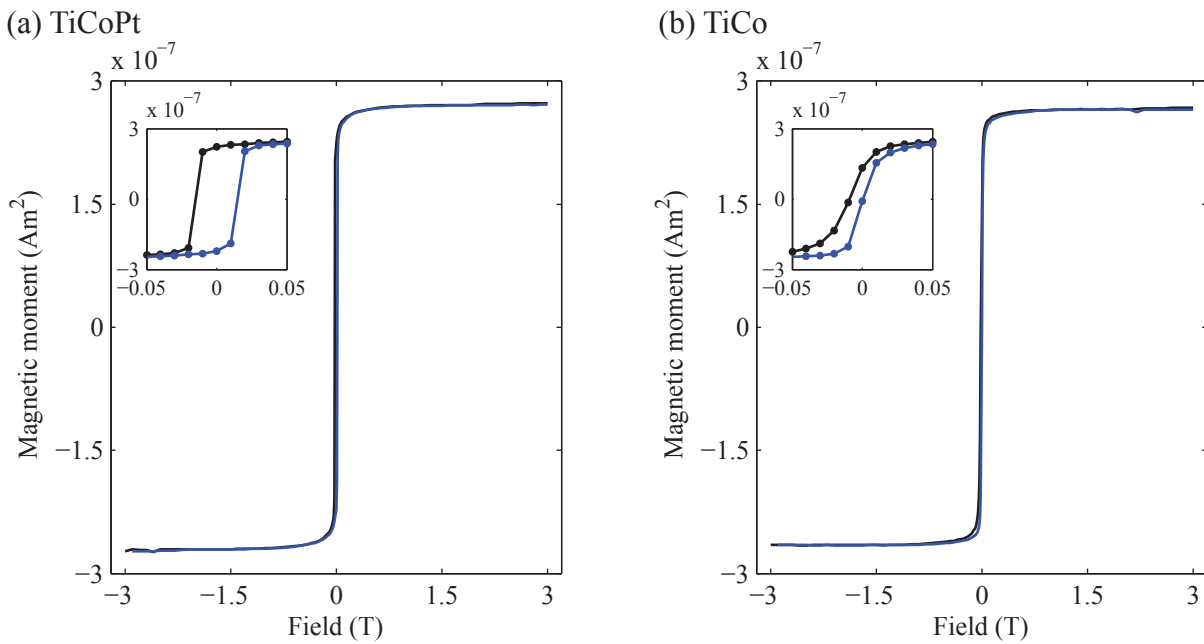


Figure 4.8: In-plane magnetization loops for platinum-capped and uncapped cobalt films obtained at 4.0 K using SQUID magnetometry and magnified views of the hysteresis near zero field. (a) Platinum-capped thin film with an 84 nm thick cobalt layer and a corresponding saturation magnetization of  $\mu_0 M_{\text{sat}} = 1.8 \pm 0.1$  T. (b) Uncapped 93 nm thick cobalt film with  $\mu_0 M_{\text{sat}} = 1.6 \pm 0.1$  T. For both films, the magnetization was swept from +3 T to -3 T (black) and then from -3 T to +3 T (blue).

were converted to saturation magnetizations of  $\mu_0 M_{\text{sat}} = 1.8 \pm 0.1$  T for the platinum-capped film (Figure 4.8(a))<sup>2</sup> and  $1.6 \pm 0.1$  T for the uncapped film (Figure 4.8(b)). The saturation magnetization error bars again represent 95% confidence intervals and account for the error in the cobalt thickness, the cobalt lateral dimensions, and the SQUID measurement. The saturation magnetization for the platinum-capped film corresponds well to the theoretical saturated magnetic moment for cobalt of 1.8 T [91]. The saturation magnetization for the uncapped film is lower than the value for bulk cobalt, indicating the possible presence of a cobalt oxide damage layer.

For the cobalt thin films, it is instructive to note the differences between the hysteresis

<sup>2</sup>Figures 4.8(a), 4.9, 4.12, and 4.13 reprinted with permission from the Supporting Information for J. G. Longenecker *et al.*, ACS Nano **6**, 9637 (2012). Copyright 2012, American Chemical Society.

observed for the platinum-capped and uncapped films, as shown in the insets in Figure 4.8(a) and 4.8(b), respectively. Specifically, the hysteresis for the unprotected film (Figure 4.8(b)) transitions slowly between positive to negative magnetic moments, whereas the transition for the platinum-capped film (Figure 4.8(a)) is abrupt. The slow transition for the unprotected film is consistent with cooling a surface-oxidized cobalt film to cryogenic temperatures in the absence of an external magnetic field[142]. If unprotected cobalt samples would be field-cooled in future experiments, an exchange bias might be observed that could confirm the presence of a cobalt oxide layer [142]. It is also possible that SQUID magnetometry could be used to determine the thickness of this damage layer; SQUID magnetometry has been used to determine that a stable oxidation layer with a thickness of 4.4 nm formed on unprotected, 100 nm thick cobalt films [143]. Even though the platinum-capped sample also was cooled in the absence of a magnetic field, the abrupt transition for the hysteresis of the protected film indicates that the platinum-capping layer may have successfully prevented the formation of nickel oxide.

### 4.3.3 XPS Sample Preparation

XPS samples were prepared on silicon substrates by blanket deposition of 80 to 100 nm thick films using a CVC SC4500 E-gun Evaporation System. To best assess the damage experienced by platinum-capped nanomagnets, which are coated with platinum on their top surface but remain unprotected on their leading edge and other side walls, XPS samples with and without platinum capping layers were prepared.

Both nickel and cobalt XPS samples were prepared. A platinum-capped nickel film was used as a calibration sample to confirm that the XPS depth profiling method for determining etch depth was consistent with the film thickness measured by AFM; additional calibration details are provided in Section 4.3.4 and Figure 4.9. Uncapped and platinum-capped nickel

films (Figures 4.10 and 4.11) were assessed within 48 hours of preparation. Uncapped and platinum-capped cobalt films were exposed to air for one week prior to analysis to assess the oxidation damage; these are labeled in Fig. 4.12 and 4.13 as the ‘unbaked’ samples. A second set of cobalt samples were exposed to air for the same period of time, but they were spin-coated with 2  $\mu\text{m}$  of 495,000 molecular weight (poly)methylmethacrylate (PMMA) resist and baked at 115°C for 40 minutes prior to analysis in order to emulate the processing conditions of the nanomagnets; these are labeled as the ‘baked’ films.

#### 4.3.4 XPS with Depth Profiling Analysis and Results

XPS in conjunction with argon ion milling was used to measure the elemental composition versus depth in nickel and cobalt films. XPS samples were analyzed using a Surface Science Instruments model SSX-100 spectrometer with monochromated aluminum  $K_{\alpha}$  X-rays (1486.6 eV) and a beam diameter of 1 mm. Photoemitted electrons were collected at a 55 degree emission angle using a hemispherical analyzer with a 150 V pass energy. Depth profiling was performed using an argon ion source with an ion energy of 500 eV (Figure 4.12), 1000 eV (Figure 4.13(baked)), or 4000 eV (all other samples); the total beam current was 1  $\mu\text{A}$  and the ion beam was rastered over a  $1.5 \times 2.5\text{ mm}$  area. Survey scans over 0 to 1000 eV were used to determine atomic composition versus depth using the following peaks: Ni 2p, Co 2p, Pt 4d (Figure 4.9) or Pt 4f (Figures 4.11 and 4.13), O 1s, Ti 2p, and Si 2s. The spectroscopic data were used to calculate atomic percent composition of the films by using the Shirley background [144] and integrating under the appropriate peaks. The count rates for the representative peaks of each element present were scaled by their relative sensitivity factors to calculate the atomic percent composition for each spectrum.

Estimation of sample composition as a function of depth was enabled by measuring the total etch depth of each ion-milled recess *ex situ* by stylus profilometry and linearly con-

verting from etch time to etch depth. To confirm that a linear conversion was appropriate, the cobalt film in Fig. 4.9 was etched through to the silicon substrate. For comparison, the relative thicknesses of the layers were measured *in situ* during deposition by a quartz crystal microbalance, and the total film thickness was measured after deposition by AFM profilometry. The layer thicknesses were determined by AFM to be  $4.1 \pm 0.05$  nm of titanium,  $81.4 \pm 1.0$  nm of cobalt, and  $8.1 \pm 0.1$  nm of platinum; the error bars for each component, which represent 95% confidence intervals, were calculated based on the error in the total film thickness and the relative thicknesses of the three layers. The thicknesses of the film layers agreed well with the depths calculated using XPS depth profiling with linear conversion from milling time to depth. Since the same process was used to convert all etch times to depth, the depth profiles for the remainder of the films should also be accurate. The etch time-to-depth conversion factors for each film were 1.8 nm/min for Fig. 4.9, 1.53 nm/min for Figure 4.10, 1.04 nm/min for Figure 4.11, 0.31 nm/min for Figure 4.12(unbaked), 0.81 nm/min for Figure 4.12(baked), 6.6 nm/min for Figure 4.13(unbaked), and 1.0 nm/min for Figure 4.13(baked).

XPS data for platinum-capped and uncapped nickel films are shown in Figures 4.10 and 4.11, respectively. For the uncapped nickel film, oxygen content was observed within 25 nm of the nickel surface and was primarily concentrated in the first 5 nm. Capping with 8 nm of platinum was observed to successfully prevent the formation of nickel oxide.

XPS data for platinum-capped and uncapped cobalt films are shown in Figures 4.12 and 4.13, respectively. To estimate the damage to cobalt nanomagnets on magnet-tipped chips, magnetic films were compared with and without exposure to the elevated temperatures of the resist bake step for the definition of the U-shaped etch pits (Section 3.6). Baked films were coated with resist and heated at 115°C for 40 min. Unbaked cobalt films without protective platinum coatings showed oxygen within the first 3 nm of the cobalt layers, and

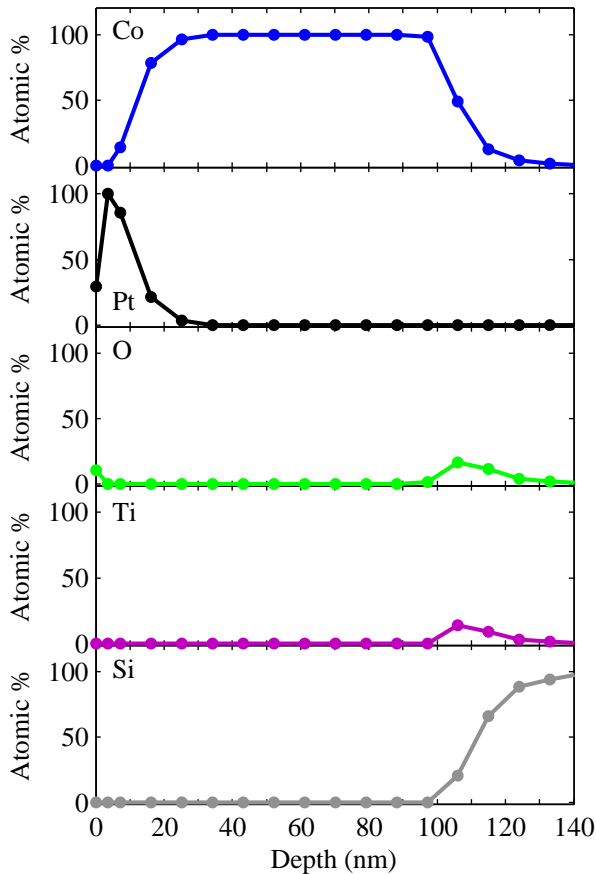


Figure 4.9: A cobalt film with a titanium adhesion layer and platinum capping layer that was evaporated onto a silicon substrate. The XPS depth profile details the atomic concentrations of cobalt (blue), platinum (black), oxygen (green), titanium (purple), and silicon (gray) as a function of depth in the film at approximately 9 nm/point spacing (data points indicated by filled circles). The depth at each point was calculated as a linear conversion of the percentage of the total time etched multiplied by the total etch depth that was measured by profilometry. The thicknesses calculated using XPS with depth profiling were compared to the thicknesses measured by the AFM-based approach discussed in the text to determine the validity of a linear conversion from etch time to depth. The thicknesses of the layers measured by the AFM-based approach were titanium ( $4.1 \pm 0.05$  nm), cobalt ( $81.4 \pm 1.0$  nm), and platinum ( $8.1 \pm 0.1$  nm), which roughly agree with the XPS thicknesses.

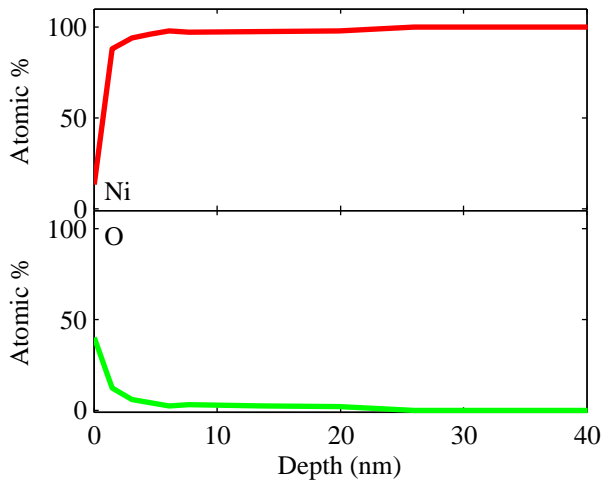


Figure 4.10: XPS depth profile of the top 40 nm of a blanket-deposited nickel film that was approximately 80 nm thick. Atomic concentrations as a function of depth are shown for nickel (red) and oxygen (green). The film was analyzed within 48 hours of deposition. Oxygen content was observed within the top 25 nm of the nickel film, with the majority of the oxygen concentrated in the top 2 to 5 nm of the film. The data indicate significant oxidation of the nickel film.

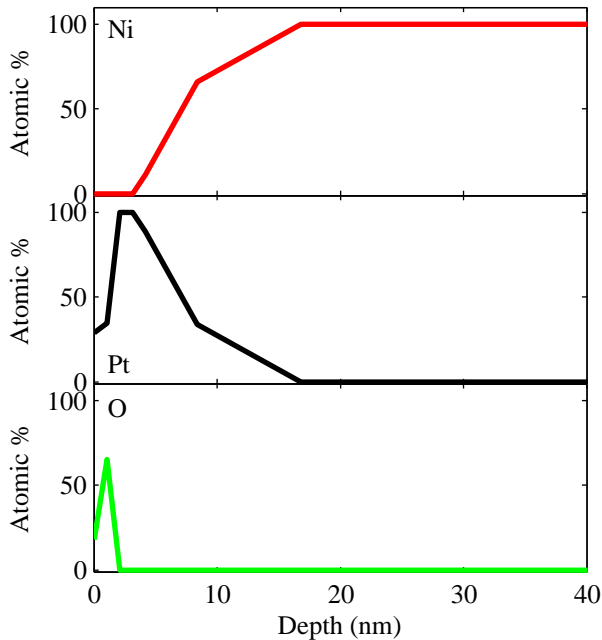


Figure 4.11: XPS depth profile of the top 40 nm of a platinum-capped, blanket-deposited nickel film. The nickel film was approximately 80 nm thick, and the platinum capping layer was approximately 10 nm thick. Atomic concentrations as a function of depth are shown for nickel (red), platinum (black), and oxygen (green). The film was analyzed within 48 hours of deposition. No oxygen was present in the nickel layer of the sample, indicating that the platinum film successfully prevented the formation of nickel oxide.

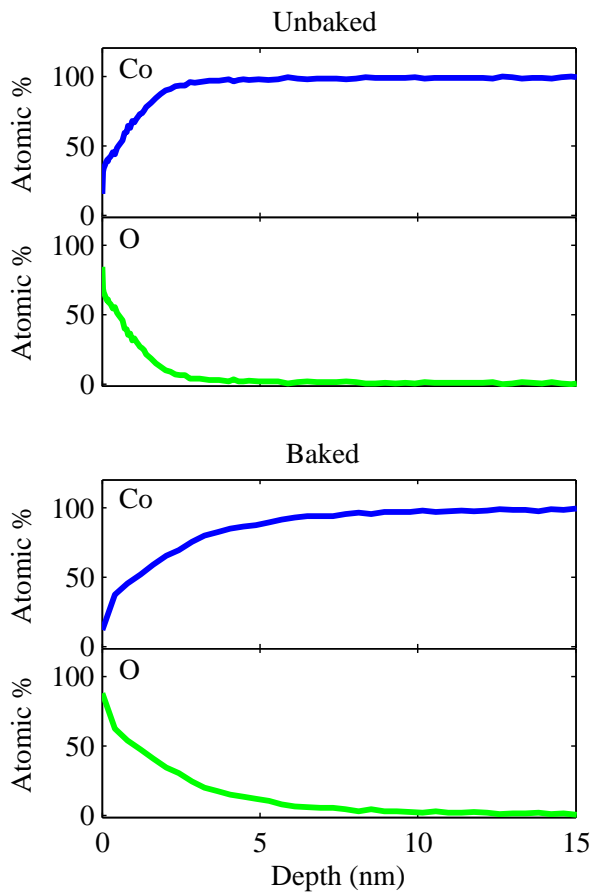


Figure 4.12: XPS depth profiles of unbaked (upper) and baked (lower) blanket-deposited cobalt films. Atomic concentrations as a function of depth are shown for cobalt (blue) and oxygen (green). The two samples were from the same wafer; both films were exposed to ambient conditions for one week prior to analysis, and the “Baked” film was coated with PMMA resist and baked at 115°C for 40 minutes in order to simulate processing damage to the leading edge of the nanomagnet studied in the manuscript.

baking the unprotected cobalt film caused an additional 2 to 9 nm of oxidation for a total oxidation depth of 5 to 12 nm (Figure 4.12). For the platinum-capped, unbaked film, a small oxygen peak was observed at the platinum-cobalt interface (Figure 4.13(a)). For the platinum-capped, baked sample, the platinum layer successfully prevented oxidation of the cobalt surface (Figure 4.13(b)).

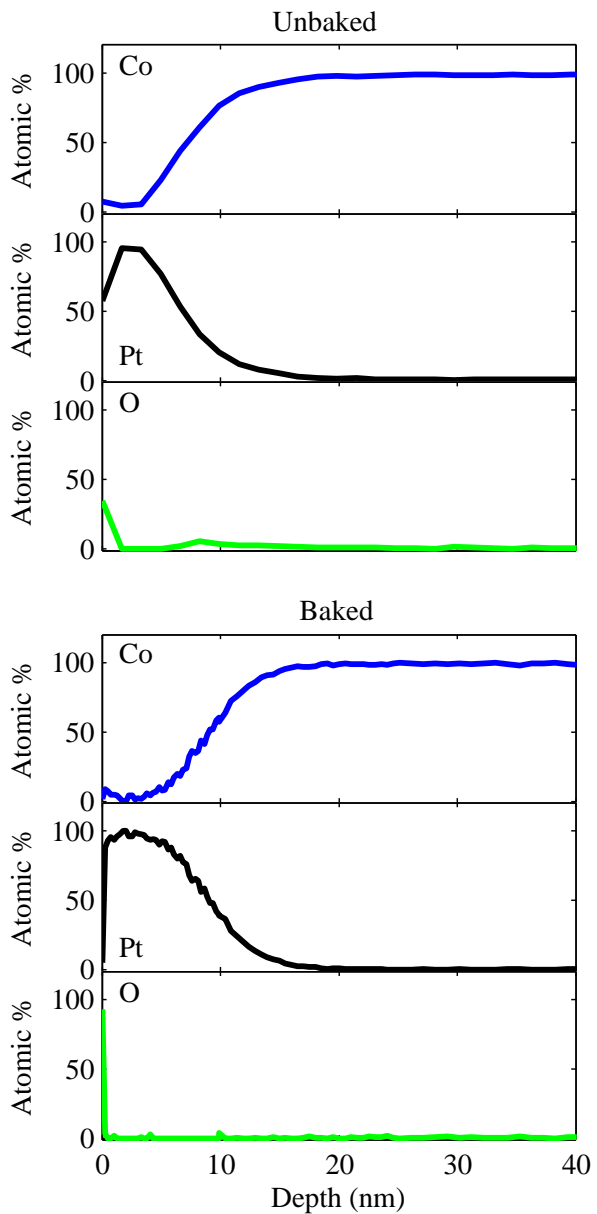


Figure 4.13: XPS depth profiles of unbaked (upper) and baked (lower) blanket-deposited cobalt films that were capped with 8 nm of platinum to mitigate surface oxidation. Atomic concentrations as a function of depth are shown for cobalt (blue), platinum (black), and oxygen (green). The two films were from the same wafer; both films were exposed to air for one week prior to analysis, and the “Baked” film was coated with PMMA resist and baked at 115°C for 40 minutes. The presence of oxygen is indicated in the cobalt layer near the cobalt-platinum interface of the unbaked film. No oxygen was observed in the cobalt layer of the baked film.

## 4.4 Reassessing Frequency-Shift Cantilever Magnetometry: Studying a Cobalt Nanomagnet

Since all magnetic and elemental analysis of the thin films indicated that the evaporated material was well-magnetized, the use of frequency-shift cantilever magnetometry was revisited, this time for a cobalt nanomagnet. The cobalt magnet — which had dimensions of  $79\text{ nm} \times 225\text{ nm} \times 1494\text{ nm}$  and was capped with 8 nm of platinum — was attached to a  $200\text{ }\mu\text{m}$  long cantilever; additional details of the magnet-tipped cantilever preparation and storage conditions prior to the measurement are provided in Section 5.2.1. Frequency-shift cantilever magnetometry measurements on the cobalt nanomagnet were conducted using a custom magnetic resonance force microscope at the IBM Almaden Research Center; the details of the microscope are provided in Refs. 12 and 60. The observed cantilever frequency shift  $\Delta f$  was converted to an equivalent magnet-induced spring constant shift using  $k_m = 2k\Delta f/f_c$ , with  $k = 1.0\text{ mN m}^{-1}$  and  $f_c = 6644\text{ Hz}$  measured as described in Section 5.2.1. The resulting data between  $-5.0\text{ T}$  to  $-0.05\text{ T}$  and  $0.05\text{ T}$  to  $5.0\text{ T}$  were fit to [93, 139]

$$k_m(B) = \mu_{\text{sat}} \left( \frac{\alpha}{l} \right)^2 \frac{B \Delta B}{B + \Delta B} + c |B|, \quad (4.2)$$

with  $B = \mu_0 H$  the applied magnetic field,  $\alpha = 1.377$  a constant for the fundamental cantilever mode,  $l = 200\text{ }\mu\text{m}$  the cantilever length, and  $\mu_{\text{sat}}$  the saturated magnetic moment.  $\Delta B = \mu_0 \mu_{\text{sat}} \Delta N/V$  is the shape-anisotropy field, with  $V$  the tip volume and  $\Delta N = N_t - N_l$  the difference in demagnetization factor along the cantilever's thickness and length, respectively. The only difference between Eq. 4.1 and Eq. 4.2 is that here the field-dependent spring constant shift of the bare cantilever at high field [89, 93] was accounted for by the term  $c |B|$ . The measured magnetic moment was converted to saturation magnetization using  $\mu_0 M_{\text{sat}} = \mu_0 \mu_{\text{sat}} / V$  with  $V = 225\text{ nm} \times 1494\text{ nm} \times 79\text{ nm}$ .

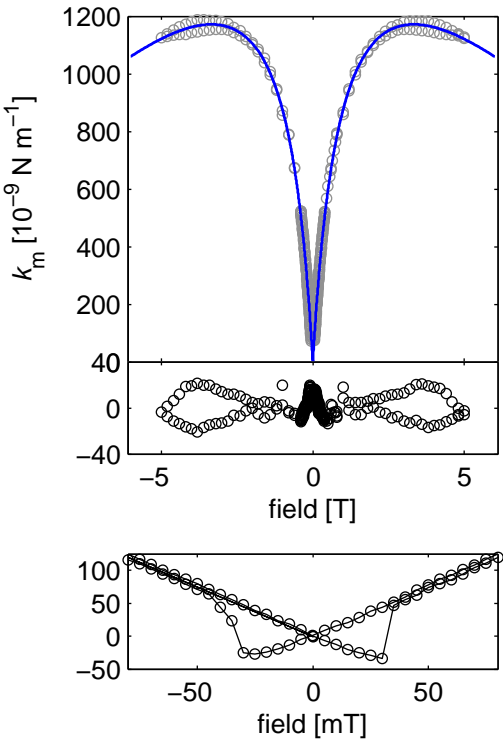


Figure 4.14: A frequency-shift cantilever magnetometry study of a cobalt nanomagnet with the applied field aligned parallel to the long axis of the nanomagnet. The external field was swept from +5 to  $-5$  T and then back from  $-5$  to +5 T. Upper: Magnetic spring constant shift  $k_m$  versus field (gray open circles) and a best fit to Eq. 4.2 (blue solid line). Middle: Fit residuals. Lower: Magnified view of the spring-constant hysteresis observed at low field.

The measured  $k_m(B)$  data shown in Figure 4.14<sup>3</sup> were well described by Eq. 4.2. The observed  $\Delta N = 0.56 \pm 0.01$  was in reasonable agreement with 0.50 expected for a high-aspect-ratio prolate ellipsoid. The observed saturation magnetization  $\mu_0 M_{\text{sat}} = 1.91 \pm 0.03$  T agreed well with 1.80 T expected for cobalt. Note that the standard error in  $\mu_0 M_{\text{sat}}$  is again reported as an indication of the goodness of fit and that the true error in  $\mu_0 M_{\text{sat}}$  is dominated by the uncertainty in  $k$ .

---

<sup>3</sup>Figure 4.14 reprinted with permission from J. G. Longenecker *et al.*, ACS Nano **6**, 9637 (2012). Copyright 2012, American Chemical Society.

## 4.5 Discussion

SQUID magnetometry measurements on large-area thin films of nickel and cobalt indicated that the evaporated material saturated at the expected value. These SQUID magnetometry findings refute hypothesis 1 in Section 4.2 that questioned whether the general-purpose evaporator used in the CNF cleanroom had induced bulk contamination of the magnetic films that reduced the saturation magnetization. XPS with depth profiling indicated that the majority of the damage to the uncapped nickel and cobalt nanomagnets was within 5 nm of the surface, and that capping with 10 nm of platinum successfully mitigated the formation of magnetic oxides. Furthermore, platinum-capped cobalt films remained intact after exposure to the elevated temperatures experienced by the nanomagnets during post-deposition processing. No elements were found to be present other than those indicated in Figures 4.9 to 4.13, indicating that the only “shell” of damage to the nanomagnets, as proposed in hypothesis 2 in Section 4.2, would be the formation of oxides. The findings presented in Section 4.3 thus indicate that the nanomagnets were damaged primarily by surface oxidation, and that the “shell” of damage was no more than 5 nm thick.

Frequency-shift cantilever magnetometry conducted on a cobalt nanomagnet showed that the saturation magnetization of  $\mu_0 M_{\text{sat}} = 1.91 \pm 0.03$  T agreed well with the value for bulk cobalt of 1.80 T. Taken together with the XPS and SQUID data on large-area thin films, these findings strongly support the conclusion that the tip exhibited a saturation magnetization close to the expected value for a fully intact cobalt nanomagnet. In contrast, frequency-shift magnetometry conducted on 120 and 220 nm wide nickel nanomagnets — even when the 40% uncertainty in the determination of the spring constant was accounted for — indicated that the magnetization of most of the tips was lower than the expected  $\mu_0 M_{\text{sat}} = 0.60$  T. The nickel magnetization had not been affected by platinum capping or by the post-deposition processing steps of overhanging the nanomagnets. Based on the comparison between the

cobalt and nickel nanomagnets, it is expected that two factors contributed to the observed low magnetization of the nickel nanomagnets. First, the nickel nanomagnets were deposited with chromium adhesion layers whereas the cobalt nanomagnet had a titanium adhesion layer. After the nickel nanomagnet study was conducted, chromium adhesion layers were found to exhibit undesired high-field magnetic behavior (Figure 4.7). The chromium high-field behavior could have impacted the saturated magnetization of the nanomagnets.

A second difference between the cobalt and nickel cantilever magnetometry measurements — and likely the primary contribution to the difference in magnetization — was that the measurements were conducted on different instruments. Frequency-shift cantilever magnetometry measurements on cobalt and nickel nanomagnets were conducted using custom-built MRFM instruments at the IBM Almaden Research Center and Cornell University, respectively. Variations between the experimental setups at IBM Almaden and Cornell may have impacted the accuracy of the measurements; specifically, the spring constant may have been more accurately measured using the instrument at the IBM Almaden Research Center. The constant  $\alpha$  in Eqs. 4.1 and 4.2 is set by the precise position of the laser interferometer reflectance off of the 30  $\mu\text{m}$  long paddle on the cantilever that is centered 67  $\mu\text{m}$  from the leading edge of the cantilever (see Figure 3.4). The large error in the determination of the spring constant is predominantly set by the difference between the laser being centered at the leading edge or far edge of this paddle. At the IBM Almaden Research Center, the position of the laser was set precisely using set screws, and thermal contraction was accounted for when adjusting the position at room temperature so that the laser was expected to be in the center of the paddle on cool down to liquid helium temperatures. The Cornell instrument used for the nickel magnetometry measurements did not have high-precision laser alignment capabilities, and no attempt was made in the Cornell measurements to account for thermal drift when aligning the fiber with the cantilever at room temperature. Additionally, low vibrational noise experienced by the IBM Almaden instrument allowed for the

measurement and comparison of the cantilever spring constant at 300 K, 77 K, and 5.5 K, whereas the spring constant was only measured in the Cornell instrument after stabilization in liquid helium at 4.2 K. The development of a new MRFM instrument with significantly improved vibration isolation is underway at Cornell University and should enable more accurate spring constant and magnetometry measurements. Details of the development of this third-generation Cornell magnetic resonance force microscope are provided in Chapter 6. For future cantilever magnetometry experiments, the additional construction of a dedicated cantilever magnetometry apparatus in which the optical fiber can be scanned at 4 K could completely eliminate errors in  $\alpha$ .

In conclusion, the nanomagnet-tipped chip on cantilever process described in Chapter 3 has been demonstrated to produce well-magnetized nanomagnets. Magnetization damage for unprotected films has been estimated to be confined primarily to within 5 nm of the surface, and oxygen contamination is mitigated by capping the magnetic material with 10 nm of platinum. Although the top surface of nanomagnets is now routinely coated with platinum because of these findings, the leading edge and other nanomagnet side walls cannot be protected using the current line-of-site evaporation technique. In MRFM experiments, the strength of the interaction between the sample spins and the nanomagnet is based on the tip-field gradient produced by the nanomagnet. The saturation magnetization of the whole nanomagnet contributes to the tip-field gradient, but the gradient is dominated by the shape of the magnet and the magnetization at the nanomagnet's leading edge. To achieve sub-nanometer MRFM imaging resolution, it will be important to reduce nanomagnet damage and/or restrict the capping layer at the leading edge to a thickness of less than 2 nm. A possible strategy to decrease the damage at the magnet leading edge would be to develop a method to encase the nanomagnet side walls with a protective coating that is less than 5 nm thick; this is discussed further in Chapter 7.

## Acknowledgements

I thank Alex Senko for his contributions to the SQUID magnetometry and XPS depth profiling data collection and analysis. I thank Eric Moore for his involvement in the nickel frequency-shift cantilever magnetometry experiments, as well as for generating code to simulate the effect of cantilever offset angle on observed magnetization. I also thank Dan Rugar and John Mamin for assistance with cobalt frequency-shift magnetometry experiments, and Jonathan Shu for assistance with the collection and interpretation of XPS data. Work in this chapter was conducted with the financial support of the National Institutes of Health (Grant No. 5R01GM-070012), the Army Research Office MultiUniversity Research Initiative (Grant No. W911NF-05-1-0403), and the National Science Foundation through the Cornell Center for Nanoscale Systems (Grant Nos. EEC-0117770 and EEC-0646547). The XPS, SQUID, and dual-beam FIB instruments used in this work are part of the Cornell Center for Materials Research, which is supported by the National Science Foundation Materials Research Science and Engineering Centers program (Grant No. DMR-0520404). Fabrication was conducted in the Cornell NanoScale Science and Technology Facility, a member of the National Nanotechnology Infrastructure Network, which is supported by the National Science Foundation (Grant No. ECS-0335765).